Journal of
Synchrotron
Radiation

ISSN 0909-0495

Received 16 June 2009
Accepted 18 August 2009

Individual GaAs nanorods imaged by coherent X-ray diffraction

Andreas Biermanns,[a]* Anton Davydok,[a] Hendrik Paetzelt,[b,c] Ana Diaz,[d] Volker Gottschalch,[c] Till Hartmut Metzger[d] and Ullrich Pietsch[a]

[a]University of Siegen, Solid State Physics Group, D-57068 Siegen, Germany, [b]Leibniz Institute for Surface Modification, Ion Beam Technology Department, 04318 Leipzig, Germany, [c]University of Leipzig, Semiconductor Chemistry Group, D-04103 Leipzig, Germany, and [d]European Synchrotron Radiation Facility, BP 220, F-38043 Grenoble, France. E-mail: andreas.biermanns@uni-siegen.de

Using scanning X-ray diffraction microscopy with a spot size of 220 × 600 nm, it was possible to inspect individual GaAs nanorods grown seed-free through circular openings in a SiN_x mask in a periodic array with 3 μm spacing on GaAs[111]B. The focused X-ray beam allows the determination of the strain state of individual rods and, in combination with coherent diffraction imaging, it was also possible to characterize morphological details. Rods grown either in the centre or at the edge of the array show significant differences in shape, size and strain state.

© 2009 International Union of Crystallography
Printed in Singapore – all rights reserved

Keywords: X-ray diffraction; coherent diffraction imaging; semiconductor nanorods; phase-retrieval analysis.

1. Introduction

Semiconductor nanorods (NRs) are of particular interest for new semiconductor devices (Thelander *et al.*, 2006). One future application is the development of one-dimensional field-effect transistors with small quantum capacity, improved power scaling and ideal linearity (Knoch *et al.*, 2008; Gunawan *et al.*, 2008). For application as light-emitting diodes it is promising that the nanorod approach can be used to form heterostructures of materials with a large lattice mismatch and to define nanorod arrays with tailored inter-rod distance (Lai *et al.*, 2008). However, all these applications require objects with uniform physical properties based on uniform morphology. To exploit effective coupling among individual nano-objects, the nanorod position has to be uniform as well.

A typical way to grow NRs is the vapour–liquid–solid growth mode on [111]B planes of zinc-blende and diamond structure compounds. In the case of catalyst-assisted growth, the size and positions of the NRs are random because both quantities are defined by the position and size of metallic catalyst droplets. One approach to overcome these drawbacks is the catalyst-free growth of NRs throughout a pre-patterned SiO_x or SiN_x mask covering a [111] substrate. By choosing appropriate growth conditions, NRs will grow preferentially inside predefined openings of the mask material. Once the openings created by electron-beam lithography and wet chemical etching are defined with regular size and distance, NRs can be grown *via* selective-area metal organic vapour phase epitaxy (SA-MOVPE) with almost uniform size forming a regular two-dimensional lattice (Hamano *et al.*, 1997; Akabori *et al.*, 2003). Using opening diameters in the range of a few hundred nanometres and inter-rod distances in the range of several micrometres, uniformly sized NR arrays have been obtained (Ikejiri *et al.*, 2007; Fan *et al.*, 2006; Paetzelt *et al.*, 2008; Tomioka *et al.*, 2008). In addition to technical advantages, NR arrays can help to understand the details of selective-area growth mechanisms. The relation between NR radius and growth rate was investigated by Paetzelt *et al.* (2008). Heiss *et al.* (2008) have demonstrated that the height of NRs grown on pre-patterned substrates is controlled by surface diffusion and desorption of group III elements. They determined a surface diffusion length L_D of 5 μm during growth by molecular beam epitaxy at 936 K.

Characterization of NR arrays is typically performed by scanning electron microscopy (SEM) providing the outer shape of individual NRs and a proof of regularity of NR arrangement. Detailed crystallographic structure characterization of single NRs has been performed by high-resolution transmission electron microscopy (TEM) so far (Larsson *et al.*, 2007). However, TEM seems not to be the method of choice for probing NR arrays because it is destructive, rather expensive in sample preparation and only a very limited number of NRs can be inspected. Alternatively X-ray diffraction has been used to obtain structural information from a statistical ensemble of non-uniform NRs or to probe individually NRs after removal from the substrate (Mandl *et al.*, 2006; Eymery *et al.*, 2007; Mariager *et al.*, 2007).

In this paper we make use of the recent achievements in X-ray optics at synchrotron radiation sources to provide an intense, coherent and focused X-ray beam that allows the selection and characterization of individual nano-sized objects using coherent diffraction imaging (CDI) (Pfeifer *et al.*, 2006;

Harder *et al.*, 2007). Up to now, CDI has been applied mostly on model systems. For example, small islands (Zozulya *et al.*, 2008) and single NRs (Diaz *et al.*, 2009; Favre-Nicolin *et al.*, 2009) were selected to demonstrate the feasibility of the method.

Here, we apply the method to an applied material science problem, *i.e.* the non-destructive structural characterization of individual GaAs NRs grown within a regular patterned two-dimensional NR array on a GaAs[111]B substrate. We will show that one can determine the shape and size of selected NRs and its lattice distortion with respect to the substrate simultaneously. Comparing NRs selected at the centre and at the edge of the array we find significant differences in shape and symmetry of the NRs which can be related to local variations in the shape of openings in the SiN_x mask or by the different lateral material flow during NR growth as predicted by Heiss *et al.* (2008).

2. Sample preparation

The GaAs NRs for this study were grown by SA-MOVPE onto a [111]B oriented GaAs substrate covered by a 15 nm-thick amorphous SiN_x layer. The silicon nitride was deposited by plasma-enhanced chemical vapour deposition at 573 K. Within an area of 250 × 250 µm the SiN_x layer was partially removed by electron-beam lithography in electron-sensitive resists followed by wet chemical etching using $NH_4F:HF:H_2O$ solution defining a square-shaped array of circular openings with diameters of 450 nm and a lateral distance of 3 µm. Selective-area GaAs growth was carried out using low-pressure (50 mbar) MOVPE in an AIXTRON AIX200 reactor with thrimethylgallium (TMGa = 3.75 ml) and arsine (AsH3 = 50 ml) as group-III and group-V material, respectively. The total flow into the reactor amounted to seven standard litres per minute (slm). The growth temperature was set to 1023 K providing equally hexagonally shaped NRs. TEM measurements on GaAs NRs grown by MOVPE show that the NRs grow predominantly in zinc-blende structure containing a large number of twins (Ikejiri *et al.*, 2008; Paetzelt *et al.*, 2008).

Prior to X-ray measurements, the NR array was inspected by SEM. Fig. 1(*a*) shows a SEM image taken close to the centre of the NR array and verifies the uniformity of the NR pattern and the regular hexagonal shape of individual NRs. The hexagonal cross section is formed by six $(1\bar{1}0)$ side facets and a top plane parallel to the substrate surface. The average height and diameter are estimated to be about 380 nm and 600 nm, respectively. At a few positions, NRs are missing owing to incomplete openings in the mask.

3. Experimental technique

The X-ray diffraction experiment was performed at the ID01 beamline at the ESRF synchrotron source using a nanofocus set-up as described by Diaz *et al.* (2009). The 8 keV X-ray beam was focused down to a spot size of 220 × 600 nm (FWHM vertical and horizontal, respectively) using a Fresnel zone plate (FZP) placed 129 mm in front of the sample position. A central beamstop and an order-sorting aperture were placed in front of and behind the FZP, respectively, to block all but the first diffraction orders produced by the FZP. In order to achieve an almost fully coherent illumination of the sample, the incoming X-ray beam was reduced to a size matching the transverse X-ray coherence lengths, both vertically (60 µm) and horizontally (20 µm). In coplanar diffraction geometry with the sample surface mounted horizontally, we measured the symmetric (111) or asymmetric (531) reflection. With the above given focal size, the final spot size on the sample surface matches well the size of individual NRs (Fig. 1*a*), allowing for an efficient use of the coherent flux. In order to identify individual NRs, we applied the technique of scanning X-ray microdiffraction (Mocuta *et al.*, 2008), taking advantage of the effect that the NR vertical lattice parameter is slightly larger (0.25%) compared with the GaAs substrate (Davydok *et al.*, 2009*a*).

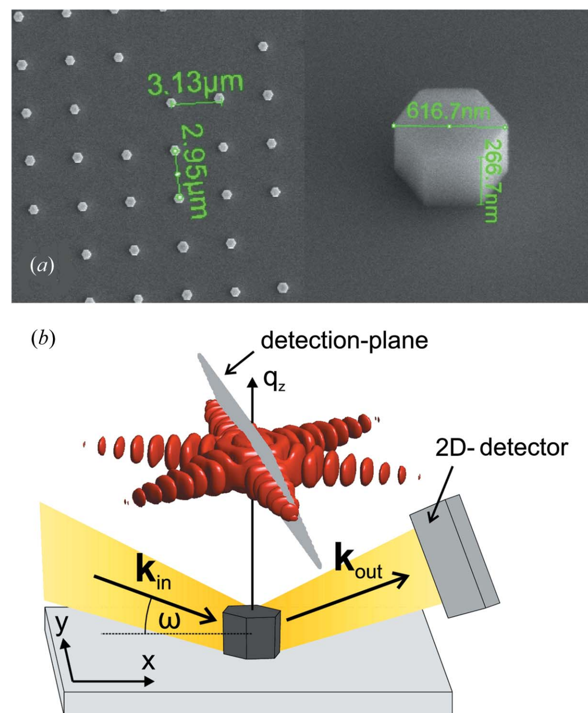

Figure 1
(*a*) SEM images displaying the regular square arrangement and hexagonal shape of NRs. (*b*) Sketch of the scattering geometry used. If a single NR is illuminated coherently, the intensity distribution around its reciprocal lattice point corresponds to the Fourier transformation of the shape (simulation in red). The two-dimensional detector covers an inclined detection plane in reciprocal space.

After fixing the incidence and exit angles of the diffracted X-ray beam to the angular Bragg position of the NR, the patterned area was scanned with nanometre precision using an *x*–*y* piezo-scanner placed below the sample. As shown later in Fig. 6(*b*), the spatial distribution of this intensity shows maxima identifying the spatial positions of individual NRs. The picture is in good agreement with the SEM image in Fig. 1(*a*), including positions of missing rods.

Based on such intensity maps we have selected four individual NRs; three close to the centre and one at the edge of

the NR array. At these selected positions we recorded three-dimensional coherent diffraction patterns in the surroundings of the GaAs (111) Bragg reflection. Fig. 1(*b*) shows a sketch of the scattering geometry used. The focused X-ray beam illuminates a single NR under an incidence angle ω close to the GaAs (111) Bragg angle. For detection of the diffracted beam we used a two-dimensional MAXIPIX pixel detector with pixel size 55 × 55 µm (Ponchut *et al.*, 2007). The centre of the detector was placed at a fixed scattering angle 2θ, covering a two-dimensional surface in reciprocal space [grey shaded plane in Fig. 1(*b*)]. The full three-dimensional intensity distribution is obtained by rotating the incidence angle ω through the Bragg position and subsequent recording of two-dimensional intensity images at each position (Williams *et al.*, 2003). For every image the intensity in reciprocal space coordinates $I(q_x, q_y, q_z)$ of each detector pixel is obtained from the incidence angle ω and the two detector coordinates defining the in-plane and out-of-plane scattering angles. Following usual definitions (Pietsch *et al.*, 2004), the q_z direction is defined parallel to the surface normal, and the plane spanned by q_x and q_y is parallel to the surface, with q_x parallel to the projection of the incident X-ray beam on the surface. Finally, the slightly non-equally spaced data in q-space were binned on a regular-spaced three-dimensional array in reciprocal space from which data visualization and the extraction of slices through the intensity distribution, *e.g.* $I(q_x, q_y, q_z = \text{constant})$, were obtained. One has to note that the measurement suffers from the restricted time-stability of a pre-aligned spatial position which was of the order of 3 h. This is the reason why complete three-dimensional images could be determined from two NRs only, the other two remained incomplete.

4. Experimental results

Fig. 2 shows a three-dimensional plot of an iso-intensity surface in reciprocal space, measured at a single rod in the centre of the patterned area around the GaAs (111) reflection.

Since the footprint of the incoming X-ray beam on the sample surface was larger than the size of an individual NR, and the penetration depth of the X-ray beam exceeds the vertical size of the rod, the Bragg peak of the substrate, located at a slightly larger q_z, is also excited. This gives rise to the vertical line of intensity which is the crystal truncation rod (CTR) of the GaAs substrate, superimposed by interference fringes from the finite NR height. Because the intensity of the substrate peak exceeds the signal of the NR by several orders of magnitude, it had to be blocked owing to the limited dynamic range of the detector, which explains the region of missing data visible in the lower part of Fig. 2, showing a slice of the diffraction pattern above through the NR signal.

Owing to the coherent illumination, the recorded diffraction pattern is the Fourier transform of the shape of the selected NR. It shows characteristic oscillations owing to its finite size and almost perfect hexagonal symmetry in the plane parallel to the surface. In order to analyze the shape of the NR, a horizontal cut through the centre of the diffraction

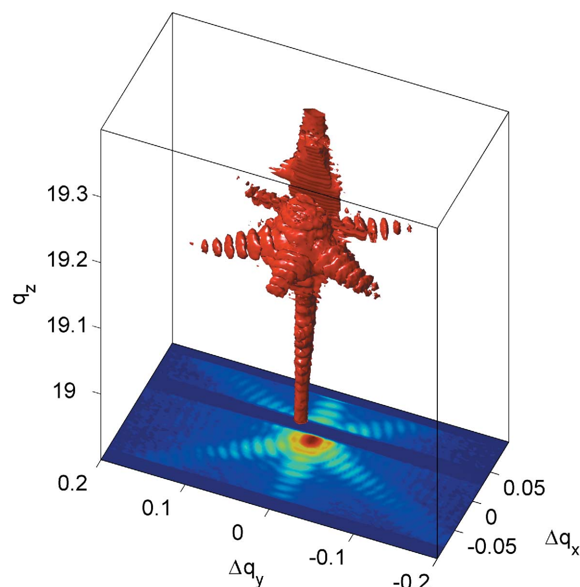

Figure 2
Three-dimensional coherent diffraction intensity distribution of a single NR close to the GaAs (111) reflection. The red structure represents an iso-intensity surface, the map below shows a cut at constant q_z through the peak from the NR. The region containing the substrate Bragg-maximum is missing in the data. All units are nm^{-1}.

pattern of the rods was extracted by summation of eight horizontal slices (total thickness along q_z: 0.018 nm^{-1}) in the q_x–q_y plane from the three-dimensional intensity distribution.

Figs. 3(*a*) and 4(*a*) show the extracted horizontal slices of a NR measured in the centre and at the edge of the array, respectively. As immediately visible, the diffraction pattern shown in Fig. 3(*a*) exhibits a shape close to that of a perfect hexagon. All the CTRs originating from the six hexagonally arranged side facets show equally spaced interference fringes. In contrast, the pattern taken at the edge of the array (Fig. 4*a*) displays a non-perfect, more deformed, hexagon. Here, the spacing between interference fringes differs along the different CTRs. The respective diameters D of the hexagon are estimated from the distances of interference maxima, $\Delta q_{\parallel}$, along a CTR by $D = 2\pi/\Delta q_{\parallel}$. It results in ~500 nm for all six CTRs of the central rod but two different diameters, *i.e.* 400 nm and 470 nm, for the NR at the edge. Although the other two three-dimensional coherent diffraction patterns are incomplete (see above), their diameters are ~500 nm as found for the NR at the centre. Fig. 5 shows a q_x–q_z cut through the three-dimensional NR pattern around the GaAs (111) reflection. It displays a modulated intensity along the CTR (insets) measuring the height, L, of the selected NR by $L = 2\pi/\Delta q_z$. For the central NR we find a value of $L = 400$ nm which is in good agreement with the height of 380 nm measured in Fig. 1(*a*), taking into account the sample inclination of 45° used for the SEM image. The respective height of the NR at the edge is $L = 360$ nm, *i.e.* 10% smaller than found for the central NR.

In addition, the tilt of the facet CTRs with respect to the vertical direction in Fig. 5(*b*) shows that the side facets of the NR at the edge are slightly tilted with respect to the substrate

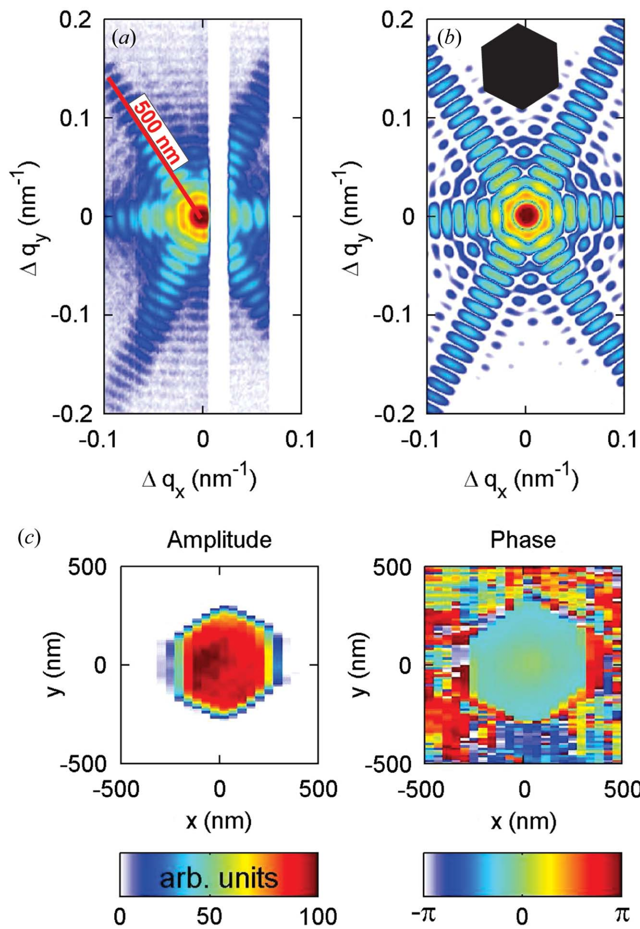

Figure 3
(a) Cut at constant q_z through the NR-(111)-signal from a NR in the centre of the array. Interference fringes measure a size of 500 nm. (b) Simulated intensity distribution obtained from two-dimensional fast Fourier transform of a homogeneous hexagon (black inset). (c) Amplitude and phase of the diffracting NR obtained by phase-retrieval analysis of the data shown in (a).

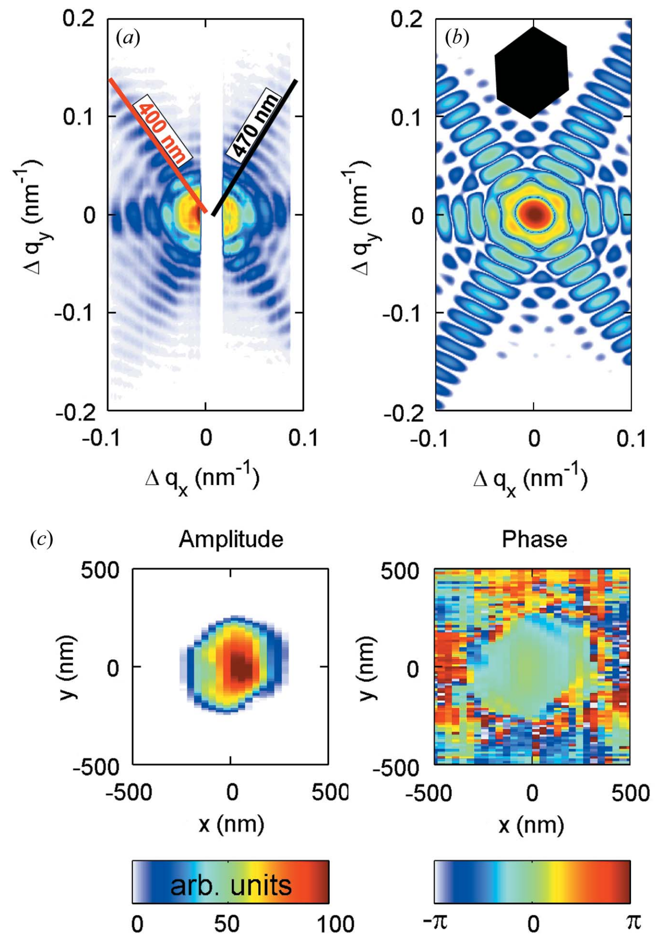

Figure 4
(a) Cut at constant q_z through the NR-(111)-signal from a NR at the edge of the array. (b) Simulated intensity distribution obtained from two-dimensional fast Fourier transform of an irregular homogeneous hexagon (black inset). (c) Amplitude and phase of the diffracting NR obtained by phase-retrieval analysis of the data shown in (a).

which lies perpendicular to the vertical CTR. This inclination angle is of the order of 4°. Furthermore, we find that the lattice mismatch, measured by the distance between the Bragg peak (indicated by the circle) and the rod's Bragg peak, differs for both NRs. It is $\Delta q_z/q_z = -0.25\%$ for the central NR and $\Delta q_z/q_z = -0.20\%$ for the edge NR. The respective values of the other NR are around −0.25% as well. In order to probe the in-plane mismatch of the NRs we performed measurements at the asymmetric (531) reflection, inclined by 28.56° with respect to the sample surface. Fig. 6(a) shows a q_x–q_z map of this reflection, measured as an ensemble average of the NR array with a 100 × 100 µm-sized beam. The intense peak at $q_z = 57.84$ nm^{-1}, $q_x = 31.18$ nm^{-1} is the substrate reflection, whereas the less intense peak at smaller q_z refers to the NRs. This peak shows a displacement of $\Delta q_z/q_z = -0.25\%$ along the vertical direction, indicating the same average strain as already found in the symmetric reflections (see above). However, the peak also shows a lateral lattice misfit of $\Delta q_x/q_x \simeq 0.1\%$ towards a smaller in-plane lattice parameter. Fig. 6(b) shows the spatial distribution of the NRs' peak intensity,

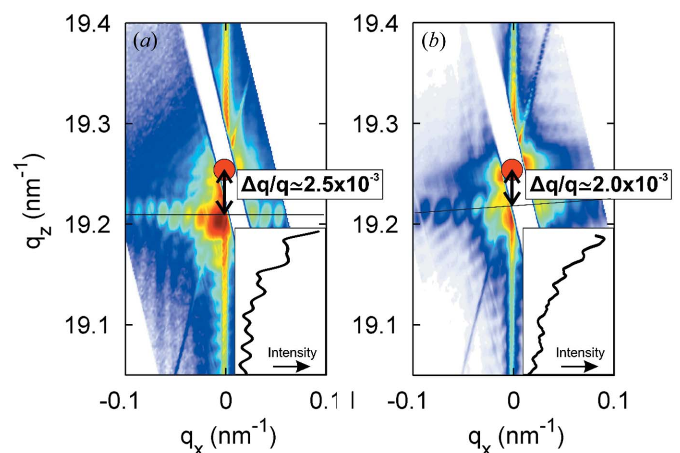

Figure 5
Cut in the q_x–q_z plane through the (111)-diffraction signal of the rod in the centre (a) and at the edge (b). Vertical lattice mismatch, tilt of the NR diffraction signal and vertical size are different in both cases. The inset shows interference fringes along the CTR, measuring the height of the NR.

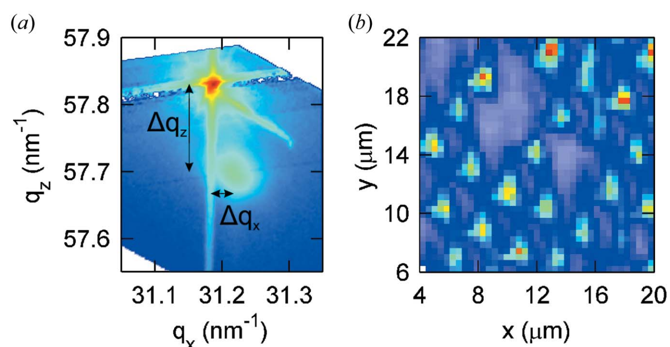

Figure 6
(*a*) Intensity distribution around the GaAs(531) reflection. The NRs' Bragg peak shows an expansion of the NRs' lattice constant along the vertical and a compression along the lateral direction. (*b*) Spatial intensity distribution of the NR peak.

measured with the focused beam. Clearly visible is the spatial distribution corresponding to individual NRs, including positions of missing NRs as already seen in the SEM image (Fig. 1*a*).

4.1. Data evaluation by Fourier transforms

The small deviation from hexagonal shape found in reciprocal space suggests a model-adapted simulation in order to extract the NR parameters in the horizontal plane. As a model we used a regular or distorted two-dimensional hexagon with homogeneous density and diameters D_i along the three hexagonal directions, and calculated the squared modulus of a two-dimensional Fourier transform. The model parameters D_i were varied to find minimum deviation from the experiment. The simulated reciprocal-space patterns are shown in Figs. 3(*b*) and 4(*b*) with the models indicated by black insets. Even the small intensity features between the main facet-streaks are well reproduced and one clearly can distinguish between regular and distorted NR shape. The NR in the centre is an almost perfect hexagon with a diameter of 500 nm, corresponding to a distance between opposite corners of 580 nm. This is in good agreement with the result from SEM analysis shown in Fig. 1(*a*). Contrarily, the NR at the border of the array (Fig. 4*b*) is considerably smaller and asymmetric, featuring four larger and almost symmetric and two shorter side planes.

4.2. Phase-retrieval analysis

Although the intuitive analysis of the object's shape using Fourier transform gives fast access to results, in this case owing to the rather simple structure of the system, the strength of the coherent diffraction technique lies in the possibility of a model-free direct imaging of the electron density of the object, provided that the oversampling criterion is fulfilled (Miao *et al.*, 1999). This is the case for the diffraction patterns shown in Figs. 3(*a*) and 4(*a*), in which fringes arising from the finite two-dimensional extension of the NRs' cross sections can be observed. Measuring close to Bragg reflections additionally opens opportunities for the measurement of atomic displacement fields within individual nanocrystals (Pfeifer *et al.*, 2006). In this method, a complex-valued object is considered, the amplitude of which represents the electron density of the object and its phase the displacement field projected onto the probed Bragg reciprocal space vector.

In order to retrieve the object directly from the measured data, we used a combination of standard phase-retrieval algorithms, namely error reduction (ER) (Gerchberg & Saxton, 1972), hybrid input–output (HIO) (Fienup, 1982) and shrink-wrap (SW) (Marchesini *et al.*, 2003). The algorithms were applied directly on the two-dimensional data shown in Figs. 3(*a*) and 4(*a*), defining a two-dimensional phasing problem. In the algorithms, both amplitude and phase in real space were allowed to evolve free, with no other constraint apart from the necessary support constraint (Fienup, 1982). An initial support was assumed from the autoconvolution function, obtained through inverse Fourier transformation of the measured intensity pattern. Successive iterations of 50 times the ER algorithm followed by 2000 times the HIO algorithm were performed. The SW method was applied every 20 iterations of the HIO algorithm, following the scheme described by Marchesini *et al.* (2003). This approach allowed the support to progressively shrink to a size slightly larger than the reconstructed object. The performance of the algorithm was considerably improved with the use of the SW approach in comparison with a classical iteration of ER and HIO algorithms. Finally, 50 iterations of the ER algorithm were performed, making a total of 4150 iterations. Following this procedure, we performed 70 reconstructions starting with different sets of random phases each time and we averaged the complex-valued solutions, as reported previously (Diaz *et al.*, 2009).

Figs. 3(*c*) and 4(*c*) show the obtained NRs' cross sections (amplitude and phase) corresponding to the diffraction patterns shown in parts (*a*) of the respective figures. The reconstructed image of the wire in the centre of the sample (Fig. 3*c*) shows a regular hexagon of equal side facets with a width of around 500 nm between opposite sides and an almost homogeneous electron density within the hexagon. On the other hand, in the second reconstruction corresponding to a NR at the edge of the array (Fig. 4*c*), the reconstructed object has the shape of an elongated hexagon along one direction, exhibiting a width of about 480 nm between the two opposite facets along this direction, while the width between two opposite facets along the other two directions is about 400 nm and 380 nm, respectively. The electron density within this NR is not homogeneous, showing a bump in the centre. Missing data in both diffraction patterns, arising from the much stronger Bragg reflection and from the substrate CTR, have been replaced by their corresponding centre-symmetric points prior to the phase-retrieval process. This effectively replaces all missing data in Fig. 3(*a*). However, this cannot be applied for all missing points in the case of Fig. 4(*a*), where some data are missing for both centre-symmetric pixel positions. Such missing data could explain the non-homogeneous electron density obtained in Fig. 4(*c*), as already reported by Diaz *et al.* (2009). The reconstructed phases show small phase changes up

to about $\delta\varphi = 0.5$ rad. In principle, one could attribute these changes to atomic field displacements along the z-direction up to about $\delta\varphi/q \simeq 0.025$ nm. However, such small phase variations have previously been obtained in systems in which they were not expected, and they might be due to a non-perfect data quality (Diaz *et al.*, 2009). Given the parabolic structure of the phase within the nanowires' cross section, one might naively think that it results from the wavefront of the incoming focused beam. Indeed, the incoming beam could very well exhibit a similar curved profile at the focal plane. However, we note that, owing to the Bragg geometry of the experiment, the focal plane is tilted by an angle of $90^\circ - \theta_B = 76.35^\circ$ with respect to the xy plane of the nanowires' cross section. Therefore, such a phase structure cannot be explained by the incoming wavefront at the sample position, but is rather due to artifacts in the experimental data.

The results obtained by phase retrieval are in perfect agreement in terms of shape and size with those reported above for the Fourier transform analysis. In addition, they show the realistic spatial resolution owing to the extension in reciprocal space of the measured diffraction patterns. In the vertical direction (y) the real-space resolution is about 15 nm, limited by the measured dynamic range in intensity. In the horizontal (x) direction a resolution of about 50 nm is obtained, limited by the range of the rocking scan around the Bragg reflection.

5. Discussion

Compared with SEM, the method applied here provides not only the NR shape but also crystallographic parameters as lattice parameters and lattice strain. Because CDI is destruction- and model-free, the method can be regarded as an alternative to high-resolution TEM. In the present case we could show that NR parameters such as height, diameter, lattice mismatch and misorientation change among NRs at different positions in the predetermined NR array. This might be caused by the fluctuation of local shape of the etched openings in the SiN_x mask and by the growth parameters. Additionally, we find significant changes of the NR shape between centre and edge in the NR array. Therefore our findings might also be caused by the difference in the area of diffusion for group III material during growth. Since the lateral NR spacing of 3 µm is much smaller than the surface diffusion length L_D of gallium at the growth temperature (Heiss *et al.*, 2008), the NR volume depends on the number of next neighbours. Whereas in the centre the adatoms are shared among four next neighbours, the NRs at the edge share the growth material with three next neighbours on one side, while the neighbours on the other side are missing, thus resulting in a non-regular shape. However, our findings display the opposite behaviour. Instead of a larger NR expected by this model we find a smaller NR at the edge compared with that at the centre. This suggests that local variations in shape and size of the openings in the mask cause the differences found in the NR shape. Moreover, the proof of the previous assumption would have required measurements at more than one border NR and investigation at different NR arrays with variable spacing.

The small fluctuation in NR orientation might be explained by local fluctuations of growth conditions and the shape of openings. Similar local fluctuations of NR orientations were found for GaAs NRs grown on Ge[111] (Davydok *et al.*, 2009*b*).

The origin of the lattice mismatch found between the GaAs NR and the GaAs substrate and its variation among the different NRs will need further investigation. The appearance of an in-plane lattice mismatch suggests a non-pseudomorphic growth between GaAs NRs and GaAs substrate. Presently it is not clear whether inclusions of mask material or a certain arrangement of stacking faults or twins at the bottom of NRs can cause the lattice mismatch. However, similar expansions of the vertical lattice parameter have been found at InAs NRs grown on InP[111]B (Mandl *et al.*, 2006). *Ab initio* theoretical calculations do not predict such lattice expansion even considering various passivations of NR side planes (Leitsmann & Bechstedt, 2007). The influence of wurtzite twinnings on photoluminescence properties in ternary II–VI compound NRs has been reported recently (Yin & Lee, 2009). The deviation from the linear relation between band gap and composition is explained by the appearance of various (013) twins. Systematic investigations between the relation of twins and stacking faults with lattice parameter do not exist. However, following the same reasons we relate the lattice mismatch in our NRs to the appearance of such twins and stacking faults. The clear understanding of this model needs further experiments.

In summary, using scanning X-ray diffraction microscopy we were able to identify and to select individual GaAs NRs grown seed-free in a periodic array with 3 µm spacing. In combination with coherent diffraction imaging, we were able to characterize morphological details of individual rods and found variations from almost perfect hexagonal to smaller and more distorted shapes, accompanied by different strain states of the NR.

References

Akabori, M., Takeda, J., Motohisa, J. & Fukui, T. (2003). *Nanotechnology*, **14**, 1071–1074.
Davydok, A., Biermanns, A., Pietsch, U., Grenzer, J., Paetzelt, H. & Gottschalch, V. (2009*a*). *Metallurg. Mater. Trans. A*, doi:10.1007/s11661-009-9868-3.
Davydok, A., Biermanns, A., Pietsch, U., Grenzer, J., Paetzelt, H., Gottschalch, V. & Bauer, J. (2009*b*). *Physica Status Solidi A*, **206**, 1704–1708.
Diaz, A., Mocuta, C., Stangl, J., Mandl, B., David, C., Vila-Comamala, J., Chamard, V., Metzger, T. H. & Bauer, G. (2009). *Phys. Rev. B*, **79**, 125324.
Eymery, J., Rieutord, F., Favre-Nicolin, V., Robach, O., Niquet, Y. M., Froberg, L., Martensson, T. & Samuelson, L. (2007). *Nano Lett.* **7**, 2596–2601.
Fan, H. J., Werner, P. & Zacharias, M. (2006). *Small*, **2**, 700–717.
Favre-Nicolin, V., Eymery, J., Koester, R. & Gentile, P. (2009). *Phys. Rev. B*, **79**, 195401.
Fienup, J. R. (1982). *Appl. Opt.* **21**, 2758–2762.

Gerchberg, R. W. & Saxton, W. O. (1972). *Optik (Stuttgart)*, **35**, 237–249.
Gunawan, O., Sekaric, L., Majumdar, A., Rooks, M., Appenzeller, J., Sleight, J. W., Guha, S. & Haensch, W. (2008). *Nano Lett.* **8**, 1566–1571.
Hamano, T., Hirayama, H. & Aoyagi, Y. (1997). *Jpn. J. Appl. Phys.* **36**, L286–L288.
Harder, R., Pfeifer, M. A., Williams, G. J., Vartaniants, I. A. & Robinson, I. K. (2007). *Phys. Rev. B*, **76**, 115425.
Heiss, M., Riedlberger, E., Spirkoska, D., Bichler, M., Abstrelter, G. & Fontcuberta i Morral, A. (2008). *J. Cryst. Growth*, **310**, 1049–1056.
Ikejiri, K., Noborisaka, J., Hara, S., Motohisa, J. & Fukui, T. (2007). *J. Cryst. Growth*, **298**, 616–619.
Ikejiri, K., Sato, T., Yoshida, H., Hiruma, K., Motohisa, J., Hara, S. & Fukui, T. (2008). *Nanotechnology*, **19**, 265604.
Knoch, J., Riess, W. & Appenzeller, J. (2008). *IEEE Electron Device Lett.* **29**, 372–374.
Lai, E., Kim, W. & Yang, P. (2008). *Nano Res.* **1**, 123–128.
Larsson, M. W., Wagner, J. B., Wallin, M., Hakansson, P., Froberg, L. E., Samuelson, L. & Wallenberg, L. R. (2007). *Nanotechnology*, **18**, 015504.
Leitsmann, R. & Bechstedt, F. (2007). *J. Appl. Phys.* **102**, 063528.
Mandl, B., Stangl, J., Martensson, T., Mikkelsen, A., Eriksson, J., Karlsson, L. S., Bauer, G., Samuelson, L. & Seifert, W. (2006). *Nano Lett.* **6**, 1817–1821.
Marchesini, S., He, H., Chapman, H., Hau-Riege, S., Noy, A., Howells, M. R., Weierstall, U. & Spence, J. (2003). *Phys. Rev. B*, **68**, 140101(R).
Mariager, S. O., Sorensen, C. B., Aagesen, M., Nygard, J., Feidenhans'l, R. & Willmott, P. R. (2007). *Appl. Phys. Lett.* **91**, 083106.
Miao, J., Charalambous, P., Kirz, J. & Sayre, D. (1999). *Nature (London)*, **400**, 342–344.
Mocuta, C., Stangl, J., Mundboth, K., Metzger, T. H., Bauer, G., Vartanyants, I. A., Schmidbauer, M. & Boeck, T. (2008). *Phys. Rev. B*, **77**, 245425.
Paetzelt, H., Gottschalch, V., Bauer, J., Benndorf, G. & Wagner, G. (2008). *J. Cryst. Growth*, **310**, 5093–5097.
Pfeifer, M. A., Williams, G. J., Vartanyants, I. A., Harder, R. & Robinson, I. K. (2006). *Nature (London)*, **442**, 63–66.
Pietsch, U., Holy, V. & Baumbach, T. (2004). *High-Resolution X-ray Scattering: From Thin Films to Lateral Nanostructures, Advanced Texts in Physics.* Berlin: Springer.
Ponchut, C., Cleacutement, J., Rigal, J.-M., Papillon, E., Vallerga, J., LaMarra, D. & Mikulec, B. (2007). *Nucl. Instrum. Methods Phys. Res. A*, **576**, 109–112.
Thelander, C., Agarwal, P., Brongersma, S., Eymery, J., Feiner, L., Forchel, A., Scheffler, M., Riess, W., Ohlsson, B., Gösele, U. & Samuelson, L. (2006). *Mater. Today*, **9**, 28–35.
Tomioka, K., Motohisa, J., Hara, S. & Fukui, T. (2008). *Nano Lett.* **8**, 3475–3480.
Williams, W., Pfeifer, M., Vartanyants, I. & Robinson, I. (2003). *Phys. Rev. Lett.* **90**, 175501.
Yin, L. W. & Lee, S. T. (2009). *Nano Lett.* **9**, 957–963.
Zozulya, A. V., Yefanov, O. M., Vartanyants, I. A., Mundboth, K., Mocuta, C., Metzger, T. H., Stangl, J., Bauer, G., Boeck, T. & Schmidbauer, M. (2008). *Phys. Rev. B*, **78**, 121304.